Academic Journal of Science and Technology
ISSN: 2771-3032 | Vol. 23, No. 3, 2026

Detection of Physicochemical Indicators in Glutinous Rice Based on Hyperspectral Multi-Feature Fusion and 1D-CNN

Yuqi Zhou[1], Haili Yang[1, 3, *], Lei Fei[1], Jing Yang[2], Hao Xia[1], Xinjun Hu[1, 3], Manjiao Chen[1, 3], Dan Huang[1], Liangliang Xie[1, 3], Haofu Han[1]

[1]School of Mechanical Engineering, Sichuan University of Science and Engineering, Yibin 644000, China
[2]School of Physics and Electronic Engineering, Sichuan University of Science and Engineering, Yibin 644000, China
[3]Brewing Science and Technology Key Laboratory of Sichuan Province, Yibin 644000, China
[*]Corresponding authors E-mail addresses: YHLsea324@163.com (Haili Yang)

Abstract: To achieve rapid and nondestructive detection of the physicochemical properties of glutinous rice, this study proposes a glutinous rice physicochemical detection method based on hyperspectral imaging technology combined with a one-dimensional convolutional neural network (1D-CNN) and multi-feature fusion. A total of 150 glutinous rice samples from six regions, including Chichuan and Northeast China, were collected. Hyperspectral cameras were used to capture spectral data in the 900–1700 nm range for modeling and comparative analysis with multiple models. The results indicated that the multi-feature fusion method within the 1D-CNN model achieved the best performance in predicting physicochemical indicators, with all R_P^2 values exceeding 0.89 and all residual predictive deviation (RPD) values greater than 3.0. Among these indicators, the prediction accuracy for moisture was the highest ($R_P^2 = 0.986$, RPD = 8.422), demonstrating excellent predictive capability and stability. In comparison, single-feature models within the 1D-CNN framework exhibited slightly inferior but still significant predictive performance: both protein and moisture showed $R_P^2 > 0.96$ and RPD > 5.0, whereas fat and starch exhibited R_P^2 values > 0.84 and RPD values > 2.5, indicating overall stable and reliable performance. The modeling results based on characteristic wavelengths were relatively lower, with R_P^2 values for protein and moisture only slightly above 0.84 and RPD values > 2.5 and R_P^2 values for fat and starch exceeding 0.72 with RPD values > 1.9, suggesting relatively weaker generalization ability. This proposed method enabled rapid and accurate detection of the physicochemical properties of glutinous rice, thereby providing an effective approach for quality evaluation and supporting the optimization of fermentation structure and flavor stability in rice-based products.

Keywords: Deep learning; hyperspectral imaging technology; multi-feature fusion; physicochemical prediction.

1. Introduction

Chinese Baijiu includes several aroma styles, with differences in raw materials and sensory characteristics [1,2]. Sauce-aroma Baijiu is commonly produced from waxy sorghum and is associated with a persistent aroma and full mouthfeel [3]. The properties of the grain entering the process matter because they affect the condition of the steamed material and the fermented grain mass. Waxy sorghum is rich in amylopectin and takes up water readily. If the grains swell excessively, the texture of the fermentation substrate can change, with possible consequences for microbial activity and flavor development [4]. Glutinous rice is used as an auxiliary raw material in some sauce-aroma Baijiu processes [5]. After gelatinization, its starch contributes to the cohesion of the grain mixture. Its effect is likely to depend on the amount and composition of the rice as well as the processing conditions, rather than on the ingredient name alone. For instance, two rice lots may have a similar appearance but differ in their starch and moisture contents; those differences would matter when the lots are stored, steamed, or mixed with sorghum. Protein and fat are also part of the raw-material composition and may contribute to variation between lots. This study does not measure the flavor of the finished liquor. Instead, it addresses an earlier and more tractable step: determining whether the principal physicochemical components of glutinous rice can be estimated rapidly and without consuming the sample. If those estimates are reliable, they can be used to compare incoming material before a brewing decision is made. We therefore focused on starch, moisture, protein, and fat, the four components measured by the reference assays in this work. The purpose is to characterize the rice itself, not to infer a sensory score for the resulting liquor. Brewing outcomes also depend on sorghum, microbes, and processing conditions.

Glutinous rice, also called Jiangmi or Jiumi [6], contains a high proportion of amylopectin and develops a sticky texture after cooking. Its composition is relevant to brewing for several reasons. Starch supplies fermentable material and contributes to the texture of the grain mixture [7,8], while moisture affects storage and subsequent processing [9]. Proteins and lipids may also influence fermentation products and the sensory properties of the liquor [10,11]. These effects depend on processing conditions; a concentration measured in raw rice cannot, by itself, predict the final liquor quality. Nevertheless, separate measurements of starch, moisture, protein, and fat can distinguish rice lots that would otherwise be grouped together by visual inspection. They also provide quantitative reference values against which a nondestructive method can be trained and tested. We selected these four indicators to examine whether hyperspectral imaging can support routine comparison of glutinous rice from different regions before it is used in Baijiu production.

Laboratory chemical assays remain the reference method

for quantifying the principal components of grain. They can provide reliable values, but preparing and testing each sample takes time and requires instruments, which limits their use for frequent screening of incoming material [12]. A chemical result also summarizes the tested material and gives little indication of where a component varies within an imaged sample [13]. Hyperspectral imaging (HSI) records a spectrum at each image location and therefore allows prediction and visualization to be considered together. Its performance, however, depends on the material, target component, spectral range, and model. Yang et al. combined HSI with machine learning to estimate nitrogen and phosphorus in hydrangea seeds. Their reported coefficients of determination were 0.947 for nitrogen and 0.827 for phosphorus, and their nutrient-status classifier exceeded 95% accuracy [14]. The two targets did not have identical prediction performance, illustrating why separate results are needed for each constituent. He et al. studied rice starch and amylose with a CNN-AdaBoost model. They selected spectral variables using iRF and the successive projections algorithm (SPA) and combined the selected bands with color features; the reported prediction-set R^2 values were 0.9931 and 0.9889 [15]. This work is relevant to the present rice study, although amylose and the four constituents considered here are not the same prediction tasks. Zhong et al. used HSI to estimate oil content in 220 oil-bearing fungus clones, with Soxtec measurements providing reference values. Their best model reported R^2 = 0.9383, RMSE = 1.7921%, and RPD = 4.0271 [16]. Li et al. examined soybean oil and fatty acids using HSI and several wavelength-selection methods. The best selected-variable model reached a reported accuracy of 0.93 for oil and linolenic acid; compared with the NIR models in that study, HSI reduced mean relative prediction error by 21.85%–48.94% [17]. Taken together, these examples show that spectral information can predict different chemical constituents, but they also show that the useful wavelengths and attainable error depend on the specific samples and responses. They do not establish in advance whether one model can predict all four glutinous-rice components accurately. The studies also differ in the information supplied to their models. The hydrangea work addressed nutrient measurements and classification; the rice starch work combined spectral and color features; the fungus and soybean studies used different reference assays and wavelength-selection strategies. Consequently, a high coefficient in one of those settings is not a benchmark that can simply be assigned to the present dataset. It is more useful to take their shared experimental logic: obtain laboratory reference values, evaluate the spectra against those values, and compare models on held-out samples. In our case, the same imaging platform was used to consider four components that differ in concentration range and spectral response.

The cited studies address different crops and response variables, so their reported accuracies cannot be transferred directly to glutinous rice. Chemical analysis remains the reference method for composition, whereas a spectral model could screen more grains without consuming them. For brewing use, the practical question is whether one set of spectral measurements can predict several components of glutinous rice with adequate accuracy. A comparison must also distinguish gains from the model architecture from gains caused by selecting a smaller set of wavelengths. We therefore compared characteristic-wavelength models with a one-dimensional convolutional neural network (1D-CNN) and evaluated whether adding a predicted physicochemical value to the spectral input improved the other predictions. The work used HSI data from six groups of glutinous rice and focused on starch, moisture, protein, and fat. All model comparisons were made against the corresponding laboratory measurements. By comparing spectral-only and multi-feature models on the same material, we aimed to identify a useful approach for screening rice before it is used as an auxiliary raw material in sauce-aroma Baijiu production. The study addresses raw-material assessment rather than fermentation outcome or the flavor of the finished liquor.

2. Materials and Methods

2.1. Sample preparation

Six varieties of glutinous rice from different production regions were selected for physicochemical analysis: Chichuan glutinous rice (CC), Northeast glutinous rice (DB), Honghu glutinous rice (HH), Thai glutinous rice, Yunnan glutinous rice (YN), and Pearl glutinous rice (ZZ). Each sample was evenly spread over a dedicated physicochemical analysis dish (diameter 120 mm; height 15 mm) and then placed on the HSI platform for detection. A total of 25 subsamples were prepared for each rice type, resulting in 150 physicochemical samples.

2.2. Acquisition of hyperspectral data

The hyperspectral data acquisition system used in this study primarily consisted of a GaiaField-N17E-HR hyperspectral camera (Jiangsu Dualwin Spectral Technology Co., Ltd., Jiangsu, China), halogen light sources, a computer, and an aluminum alloy support frame (Fig. 1). The hyperspectral camera provided a spatial resolution of 640 × 666 pixels and a spectral resolution of 5 nm, covering the 900–1700 nm wavelength range with 512 continuous spectral bands.

While acquiring laboratory data, the collected hyperspectral images were often impacted by substantial noise due to dark current in the camera and nonuniform light intensity distribution from the illumination system; thus, the raw images cannot accurately represent the true characteristics of the samples [18] . Therefore, prior to data collection, white and black reference images were acquired to perform black–white calibration. This effectively reduced the influence of camera noise and uneven illumination, thereby achieving a relatively stable spectral reflectance [19]. The black–white calibration of the original image was calculated using Equation (1).

$$L_C = \frac{L_O - L_D}{L_W - L_D} \tag{1}$$

In this formula, L_C represents the calibrated hyperspectral image, L_O denotes the original (uncalibrated) hyperspectral image, L_W is the white reference image, and L_D is the black reference image.

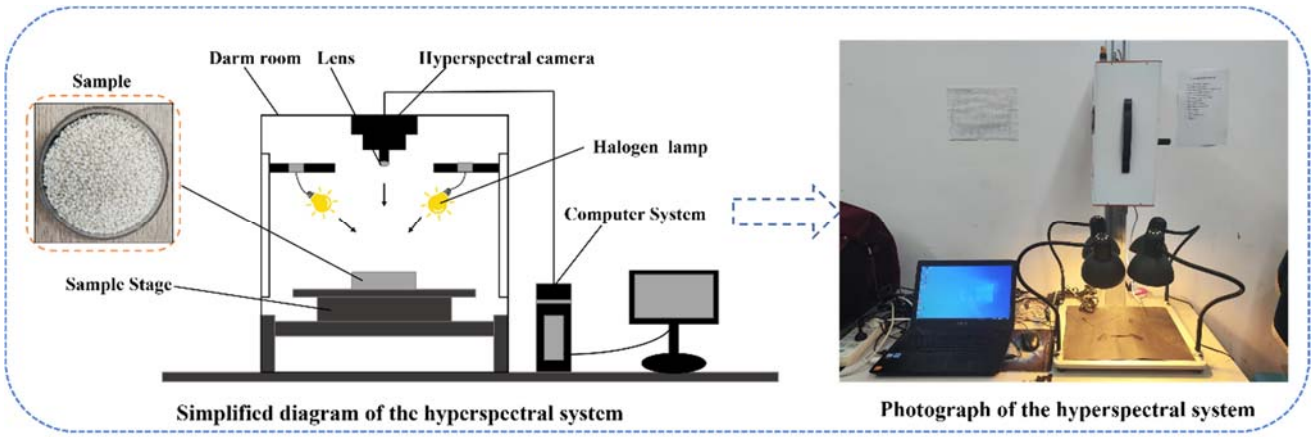


Figure 1. Hyperspectral imaging data acquisition system

2.3. Spectral data preprocessing and characteristic wavelength selection

The measured spectra can contain baseline shifts and noise from the imaging system, so preprocessing can change the information available to a prediction model. We compared min–max normalization, standard normalization, and the Box–Cox transformation rather than assuming that one treatment was suitable for every component [20,21]. The first two rescale spectral values in different ways, whereas the Box–Cox transformation changes the distribution of the values before modeling. The camera also records many wavelength channels, including neighboring channels that can contain similar information. Retaining every channel increases the number of inputs without necessarily improving prediction, particularly when the sample count is limited. Competitive adaptive reweighted sampling (CARS) and the successive projections algorithm (SPA) were therefore used to select characteristic wavelengths [22]. CARS selects variables according to their contribution to a calibration model, while SPA seeks a subset with reduced collinearity. We assessed the selected bands through the downstream prediction results for each target; the number of retained wavelengths alone was not treated as evidence of a better model. Each treatment was evaluated with the same measured component values, so the comparison concerns prediction rather than the apparent smoothness of a processed spectrum. We assessed each component separately because its useful wavelengths may differ. A subset chosen for one target could omit bands that inform another target.

2.4. Construction of physicochemical prediction model for glutinous rice

2.4.1. Support vector regression

Support vector regression (SVR) was included as a conventional nonlinear regression baseline for the spectral data [23]. SVR fits a function while allowing errors within a specified insensitive interval; deviations outside that interval contribute to the optimization objective. The penalty and kernel settings determine the balance between fit and model complexity. In this study, SVR provided a reference against which the characteristic-wavelength and 1D-CNN results could be compared. Its role was to test how well the selected spectral information predicted continuous values for the four measured components, rather than to establish a general advantage of one algorithm across all materials.

2.4.2. Extreme gradient boosting

Extreme gradient boosting (XGBoost) was used as a tree-based comparison model [24]. It builds an ensemble by adding trees sequentially, with each tree correcting part of the remaining prediction error. Its objective includes a regularization term, which can limit the complexity of the trees and the risk of fitting noise. Subsampling of rows or columns can further reduce dependence on individual samples or wavelengths. These features are relevant when many spectral channels are available relative to the number of rice samples. Unlike the 1D-CNN, XGBoost does not apply convolution along the wavelength axis to learn local spectral patterns. Comparing their results therefore helps assess whether the observed performance depends on the selected input variables or on the model used to process them. The final XGBoost prediction is the sum of the outputs of its component trees, as expressed in Equation (2).

$$y_i^{(k)} = \sum_{k}^{K} f_k\left(x_i\right) \tag{2}$$

Where, $y_i^{(k)}$ represents the final result, K denotes the total number of trees, $f_k\left(x_i\right)$ and stands for the prediction result of the k-th tree.

2.4.3. Prediction method based on 1D-CNN and multi-feature fusion

The multi-feature model was built in two stages. First, a model using the original spectral data generated a predicted value for each physicochemical indicator. For the second stage, one selected predicted value was appended to the spectrum used to predict another indicator with a 1D-CNN. This design tests whether an estimate of one component adds information that the spectrum alone does not provide for a different target. We considered different choices of the added value because the four measured components are correlated, but correlation by itself does not guarantee a gain in prediction. Figure 2 shows the network used in the second stage. A one-dimensional convolution moves along the wavelength sequence and combines signals from neighboring bands into learned features [25]. Activation and pooling operations transform those features before the fully connected layers produce a concentration estimate. The same target was evaluated with and without the added predicted value, so the benefit of the fusion input could be judged from the prediction-set metrics. This comparison is especially useful for starch and fat, whose spectral-only results were weaker than those for protein and moisture.

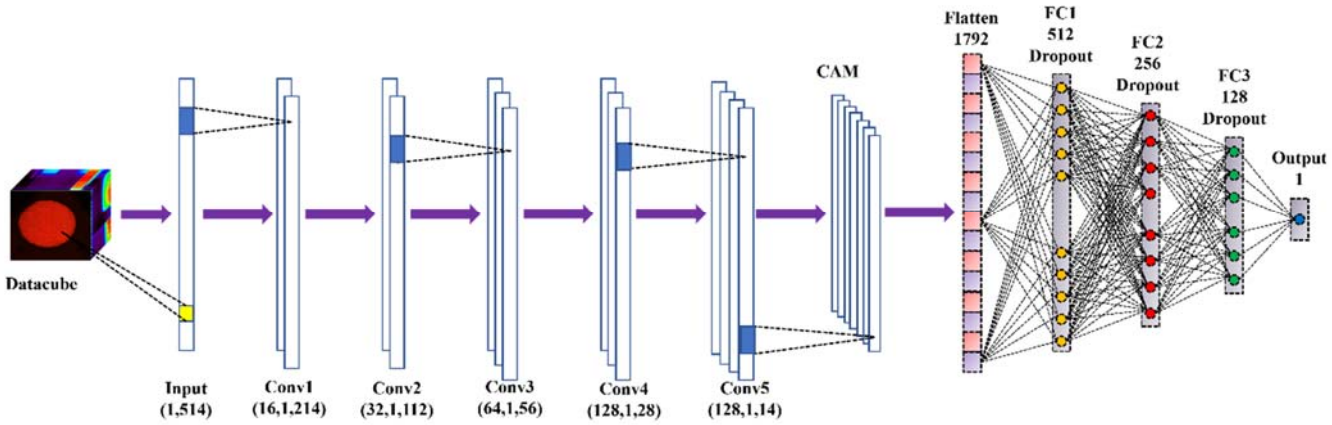


Figure 2. Structure of the one-dimensional convolutional neural network (1D-CNN) model.

2.5. Evaluation indicators of the model

All four targets were treated as continuous variables, so the model evaluation compared predicted concentrations with the corresponding laboratory measurements [26]. We used six parameters: coefficients of determination for the calibration and prediction sets (RC2 and RP2), root mean square errors for those sets (RMSEC and RMSEP), residual predictive deviation (RPD), and ABRMSE. RC2 and RMSEC describe fit on the calibration samples; RP2 and RMSEP describe how well the resulting model predicts samples held out for evaluation. RPD relates the spread of the reference values to prediction error. It is read together with RP2 because a single statistic can conceal differences in how errors are distributed across the samples. A value above 2.5 was used as a practical reference point in comparing models, not as a substitute for examining the other metrics. ABRMSE is the absolute difference between RMSEC and RMSEP. A small difference is consistent with similar errors in the two sets, although it does not identify why errors arise or prove that the model will transfer to other rice batches. The calculation formulas are given in Equations (3)–(6).

$$R^2 = \sum_{i=1}^{n}\left(\hat{Y}_i - Y_i\right)^2 / \sum_{i=1}^{n}\left(\hat{Y}_i - \overline{Y}\right)^2 \quad (3)$$

$$RMSE = \sqrt{\frac{1}{n}\sum_{i=1}^{n}\left(\hat{Y}_i - Y_i\right)^2} \quad (4)$$

$$RPD = \frac{1}{\sqrt{1 - R_p^{\,2}}} \quad (5)$$

$$AB_{RMSE} = \left|RMSEC - RMSEP\right| \quad (6)$$

In the formula, $\hat{Y}_i$ and Y_i represent the predicted and measured content of the target component for the i-th glutinous rice sample, respectively; $\overline{Y}$ denotes the average value of the target component content in the glutinous rice sample set; n stands for the number of samples in the calibration set or prediction set.

2.6. Visualization of physicochemical content

The physicochemical content maps were used to inspect how predicted values varied across the imaged glutinous rice samples [27]. Each map places a content estimate at the corresponding image location, making within-sample variation visible alongside differences between samples. Such maps complement the numerical model metrics: a model can have a favorable average prediction error while still showing uneven spatial patterns. We therefore used the maps as a visual check of the predicted distribution of protein, moisture, fat, and starch. The colors indicate relative content according to the scale shown in the figure; they should be read together with the model's prediction accuracy rather than treated as independent chemical measurements.

3. Results and Analysis

3.1. Analysis of spectral characteristics

The average spectral reflectance of glutinous rice samples from different regions is shown in Figure 3. As observed in the spectral curves within the 900–1700-nm range, the overall trends of the curves were similar among the samples, indicating that their primary chemical compositions and structural characteristics were alike. Within the wavelength range of 920–1150 nm, the spectral curves exhibited an upward trend, with a distinct absorption peak appearing at approximately 970 nm, which was mainly associated with the overtone of the O–H stretching vibration of water [28]. In the range of 1150–1480 nm, the curves displayed a clear downward trend, with noticeable absorption peaks around 1230 and 1450 nm. Beyond 1450 nm, the spectral curves gradually leveled off. The absorption peak near 1220 nm was primarily related to the second overtone absorption of C–H bonds [29] , whereas the absorption peak around 1470 nm was mainly attributed to the combination band absorption of O–H bonds [30] .

Different preprocessing methods were applied to the original spectral data in this study to further reduce spectral noise interference and improve the accuracy of spectral data modeling, as shown in Figure 4. Panels (a)–(d) correspond to the original spectral data, min–max normalization (Min-Max), standardization (Standard), and Box–Cox transformation preprocessing, respectively.

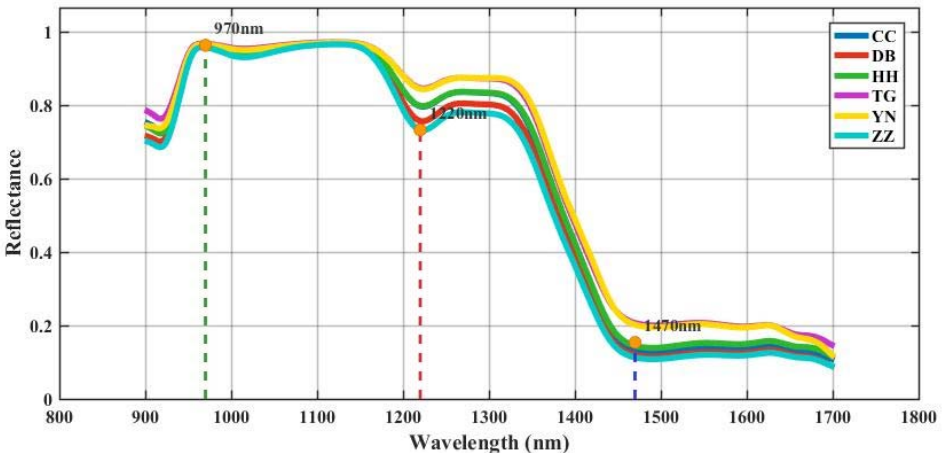


Figure 3. shows the average spectral curves

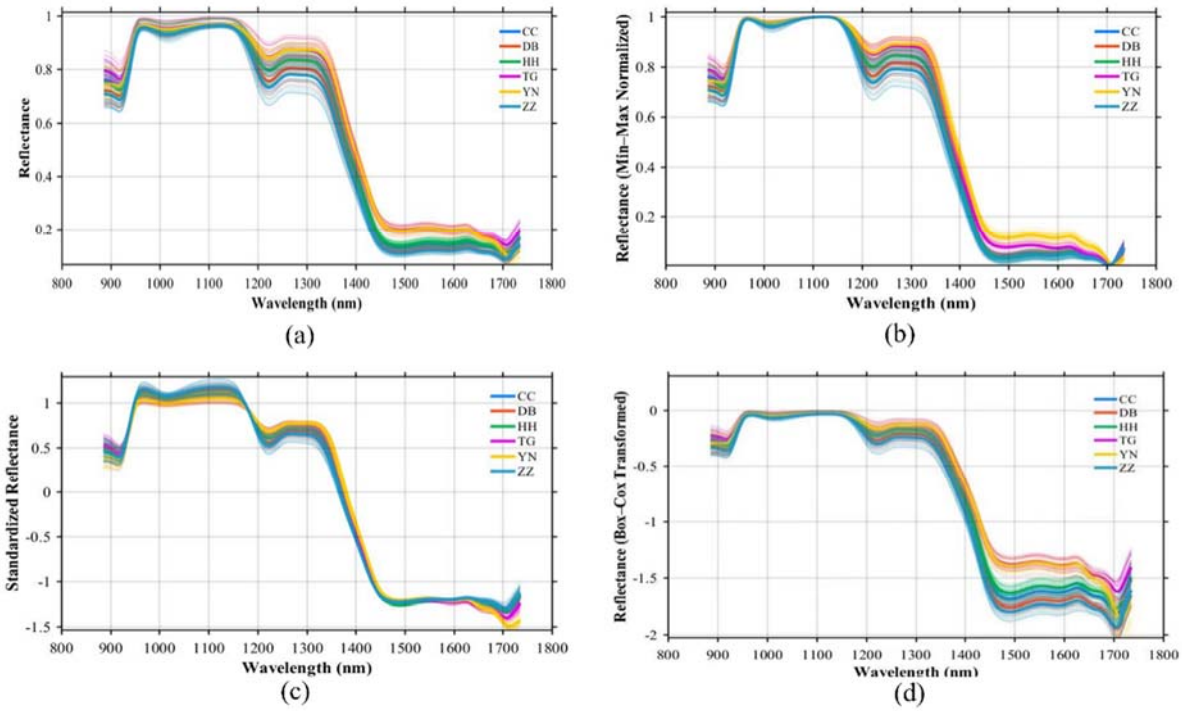


Figure 4. shows the original spectral curves and those obtained after different preprocessing methods

3.2. Modeling results based on characteristic wavelengths

Feature wavelength extraction was carried out for the two models under the optimal preprocessing conditions to further improve the generalization performance of the model. The results are shown in Table 1. The model accuracy and stability were effectively improved after combining CARS feature wavelength extraction with the optimal preprocessing combinations (SVR-Standard and XGBoost-Min–Max). For the protein index, both R_P^2 and RPD increased significantly after feature extraction, with the SVR-Standard-CARS exhibiting the most outstanding optimization effect. The moisture model maintained strong generalization ability before and after extraction; specifically, the RPD increased to 3.645, further enhancing stability. The starch model performance improved slightly, which might be related to the complexity of its spectral response. In the fat model, SVR-Standard performed better than XGBoost-Min–Max before extraction, whereas the R_P^2 and RPD of the latter increased to 0.705 and 1.841, respectively, after extraction, displaying a significant improvement. In comparison, the effect of SPA feature extraction on model performance varied remarkably. Only the moisture model performance improved, with the R_P^2 and RPD of XGBoost-Minmax-SPA increasing to 0.954 and 4.674, respectively, whereas the optimal protein model performance decreased significantly after SPA processing. The starch model performed poorly due to the complexity of the spectral signals and the fewer extracted wavelengths. In the fat model, XGBoost-Minmax-SPA improved slightly, but the SVR-Standard-SPA performance declined. Overall, CARS feature wavelength extraction can effectively remove redundant spectral information and improve the prediction accuracy and generalization ability of models for physicochemical indicators, whereas SPA presents a risk of missing key features in some components, leading to a decline in model performance.

Table 1. shows the extraction results based on feature wavelengths (CARS and SPA)

Physchem	Model	Training Set		Test Set		RPD	AB_RMSE
		R_C^2	RMSE	R_P^2	RMSE		
Protein	SVR-Standard	0.8746	0.1271	0.6541	0.2792	1.7003	0.1521
	XGBoost-Minmax	0.9513	0.0810	0.7446	0.2357	1.9786	0.1547
	SVR-Standard-CARS	0.8973	0.1173	0.8423	0.1933	2.5179	0.0760
	XGBoost-Minmax-CARS	0.9562	0.0786	0.7832	0.2134	2.1476	0.1348
	SVR-Standard-SPA	0.8613	0.1335	0.6402	0.2865	1.6671	0.1530
	XGBoost-Minmax-SPA	0.8707	0.1318	0.4051	0.3489	1.2965	0.2171
Moisture	SVR-Standard	0.9693	0.2502	0.9263	0.3151	3.4558	0.0649
	XGBoost-Minmax	0.9924	0.1244	0.9146	0.3183	3.4229	0.1939
	SVR-Standard-CARS	0.9726	0.2374	0.9247	0.2902	3.6451	0.0528
	XGBoost-Minmax-CARS	0.9478	0.3277	0.9057	0.3238	3.2569	0.0039
	SVR-Standard-SPA	0.9803	0.2017	0.9046	0.3241	3.2374	0.1224
	XGBoost-Minmax-SPA	0.9953	0.0996	0.9542	0.1962	4.6743	0.0966
Starch	SVR-Standard	0.5276	3.3952	0.6911	2.7592	1.7993	0.6360
	XGBoost-Minmax	0.7945	2.2376	0.4244	3.7692	1.3181	1.5316
	SVR-Standard-CARS	0.5727	3.2300	0.7239	2.6027	1.9032	0.6273
	XGBoost-Minmax-CARS	0.9320	1.2908	0.6481	2.9111	1.6857	1.6203
	SVR-Standard-SPA	0.4699	3.5952	0.5634	3.2856	1.5134	0.3096
	XGBoost-Minmax-SPA	0.8673	1.7999	0.4634	3.6319	1.3652	1.8320
Fat	SVR-Standard	0.8759	0.0264	0.7032	0.0387	1.8356	0.0123
	XGBoost-Minmax	0.7377	0.0391	0.3865	0.0498	1.2767	0.0107
	SVR-Standard-CARS	0.8713	0.0271	0.7212	0.0361	1.8937	0.0090
	XGBoost-Minmax-CARS	0.8098	0.0327	0.7048	0.0378	1.8407	0.0051
	SVR-Standard-SPA	0.9087	0.0226	0.6548	0.0421	1.7020	0.0195
	XGBoost-Minmax-SPA	0.7088	0.0406	0.5601	0.0460	1.5078	0.0054

3.3. Analysis of prediction results based on 1D-CNN and multi-feature fusion

3.3.1. Verification of the correlation of physicochemical components

The aforementioned spectral feature analysis showed an overlap of the absorption bands of various physicochemical components, which may complicate prediction of each component. Considering that the differences in prediction performance may be related to intrinsic correlations among the components, Pearson correlation coefficients were further used to analyze the relationships among the measured physicochemical indices [31]. The results are shown in Figure 5. The left panel presents a correlation heatmap of the four physicochemical properties. Moisture was positively correlated with protein (R = 0.78) and starch (R = 1.00), with higher moisture values accompanied by higher protein and starch values in these samples. Fat showed a negative correlation with moisture (R = −0.81), protein (R = −0.99), and starch (R = −0.81), showing an inverse association with the other three components in the measured samples. Protein and starch are also positively correlated (R = 0.79), although this compositional association does not alone establish a shared spectral response. The right panel shows a bar chart of correlation intensities. Taking the zero scale line as the boundary, moisture, protein, and starch exhibited positive correlations across the samples, consistent with the heatmap. In contrast, fat was negatively correlated with the other three components, indicating an inverse association in this dataset rather than a causal effect of fat. Among these, the correlation coefficient between protein and starch was 0.79, which motivated testing whether predicted protein could aid the other models. The strength of these associations also depends on the range of reference values represented in this sample set.

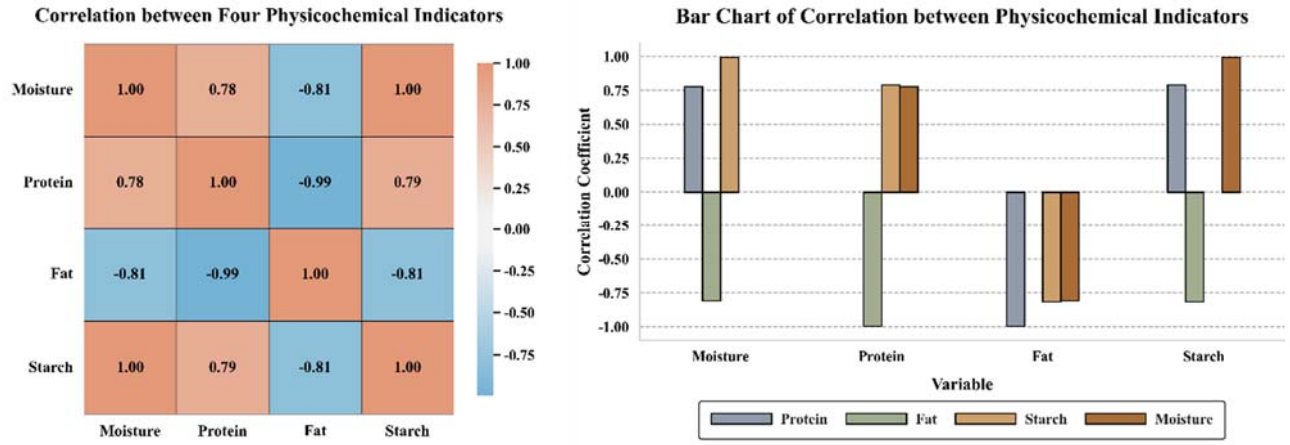


Figure 5. Verification Results of Correlation Between Physicochemical Components

3.3.2. Analysis of prediction results from multi-feature fusion

The Pearson correlation coefficient analysis showed associations among the four measured components, which suggested that a predicted component value might carry information useful for another target. To test that possibility, Table 2 presents the results of both individual predictions and feature-fusion predictions. The individual prediction results showed excellent performance for protein and moisture, with R_P^2 values in the test set both exceeding 0.96 and RPD values of 5.496 and 7.959, respectively. In contrast, the prediction performance for starch and fat was relatively weaker, with R_P^2 values above 0.84 and RPD values of 2.562 and 2.981, respectively. These values provide the spectral-only baseline against which the fusion models were compared. The fusion prediction results showed that Fusion (1) integrated the predicted values of protein into the spectral data of other physicochemical components. Compared with individual predictions, the prediction accuracy of all components increased, particularly for starch, whose R_P^2 value increased from 0.848 to 0.914 and RPD value from 2.562 to 3.415, showing an improvement in the reported prediction-set metrics. When the predicted values of protein, fat, and starch were collectively used to model moisture, its RPD value further increased to 8.422, on the same prediction set. The improvement may reflect shared information in the protein and starch responses, although this experiment did not isolate a single mechanism. The additional feature was useful in Fusion (1), as shown by the prediction-set results. In contrast, the overall model performance declined under Fusion (2), Fusion (3), and Fusion (4). One possible explanation is that predicted inputs carry error or overlap with information already in the spectrum; the negative correlations involving fat do not by themselves identify the cause. The comparison therefore supports protein-based fusion for this dataset without establishing that it is optimal for other rice batches.

Table 2. Individual Prediction and Multi-Feature Fusion Prediction Results

Model	Method	Physchem	Training Set		Test Set		RPD	AB_RMSE
			R_C^2	RMSE	R_P^2	RMSE		
1DCNN	Single	Protein	0.952	0.079	0.967	0.086	5.496	0.007
		Moisture	0.992	0.129	0.984	0.116	7.959	0.013
		Starch	0.928	1.331	0.848	1.922	2.562	0.591
		Fat	0.905	0.023	0.887	0.022	2.981	0.001
	Fusion (1)	Protein(Fat)	0.968	0.013	0.893	0.023	3.052	0.010
		Protein+Fat(Starch)	0.934	1.279	0.914	1.399	3.415	0.120
		Protein+Fat+Starch(Moisture)	0.994	0.109	0.986	0.152	8.422	0.043
	Fusion (2)	Moisture(Starch)	0.896	1.598	0.820	2.096	2.358	0.498
		Moisture+Starch(Fat)	0.914	0.022	0.830	0.029	2.427	0.007
		Moisture+Starch+Fat(Protein)	0.918	0.108	0.943	0.114	4.179	0.006
	Fusion (3)	Fat(Moisture)	0.991	0.138	0.975	0.149	6.335	0.011
		Fat+Moisture(Starch)	0.893	1.615	0.813	2.120	2.315	0.505
		Fat+Moisture+Starch(Protein)	0.875	0.133	0.942	0.115	4.147	0.018
	Fusion (4)	Starch(Protein)	0.943	0.091	0.917	0.136	3.461	0.045
		Starch+Protein(Fat)	0.924	0.021	0.860	0.027	2.671	0.006
		Starch+Protein+Fat(Moisture)	0.988	0.150	0.982	0.173	7.405	0.023

Figure 6 compares observed concentrations with predictions from the protein-based fusion configuration. For moisture, the points are clustered near the 1:1 line, in agreement with the high prediction-set RPD reported in Table 2. The fat and starch plots show more visible spread around the line, so the improvement in their summary metrics does not imply equally small errors for every sample. Protein also remains well predicted after fusion. These plots are useful because they show the distribution of individual errors rather than only an average value. A systematic departure from the diagonal would point to bias that might be hidden by a single coefficient. In the present samples, the visual pattern is broadly consistent with the ranking in Table 2: moisture is predicted most closely, while fat and starch remain more difficult. The plot supports the use of predicted protein as an additional feature in this comparison, but it does not show whether the ranking would remain the same for independently collected rice.

3.4. Result comparison and visual analysis of physicochemical indicators

Figure 7 illustrates the core performance metrics (evaluated using R^2 and RPD) of the prediction models under different types of prediction to compare the four targets on the prediction set. RPD was considered alongside R2, with 2.5 used as a practical reference value. The figure shows good performance of the individual prediction results for each physicochemical component in terms of both R^2 and RPD. Protein and moisture performed the best: R^2 values reached 0.967 and 0.984 and RPD values reached 5.50 and 7.96, respectively—showing the strongest prediction-set results among the four targets. When the predicted values of each physicochemical indicator were incorporated as output features into the spectral data, the results showed that using the predicted protein value as an output feature led to an overall improvement in R^2 and RPD values for all indicators compared with individual predictions. Specifically, the R^2 and RPD values of moisture increased to 0.986 and 8.42, those of fat increased to 0.893 and 3.05, and those of starch increased to 0.914 and 3.42; the most pronounced improvement was observed in the starch model. In contrast, when the predicted values of other physicochemical indicators (e.g., moisture, starch, or fat) were used as output features for fusion prediction, the overall prediction accuracy decreased compared with individual predictions. Because the added features were themselves predictions, their errors may have

contributed to the lower metrics; the present analysis does not isolate the cause. The four fusion inputs thus did not behave interchangeably when combined with the same spectral data. Predicted protein was the most useful additional input among the configurations tested here. The other predicted inputs produced weaker overall results, although redundancy has not been demonstrated as the sole explanation. Protein-based fusion is therefore the configuration to carry forward for independent validation, rather than a general rule for all rice samples.

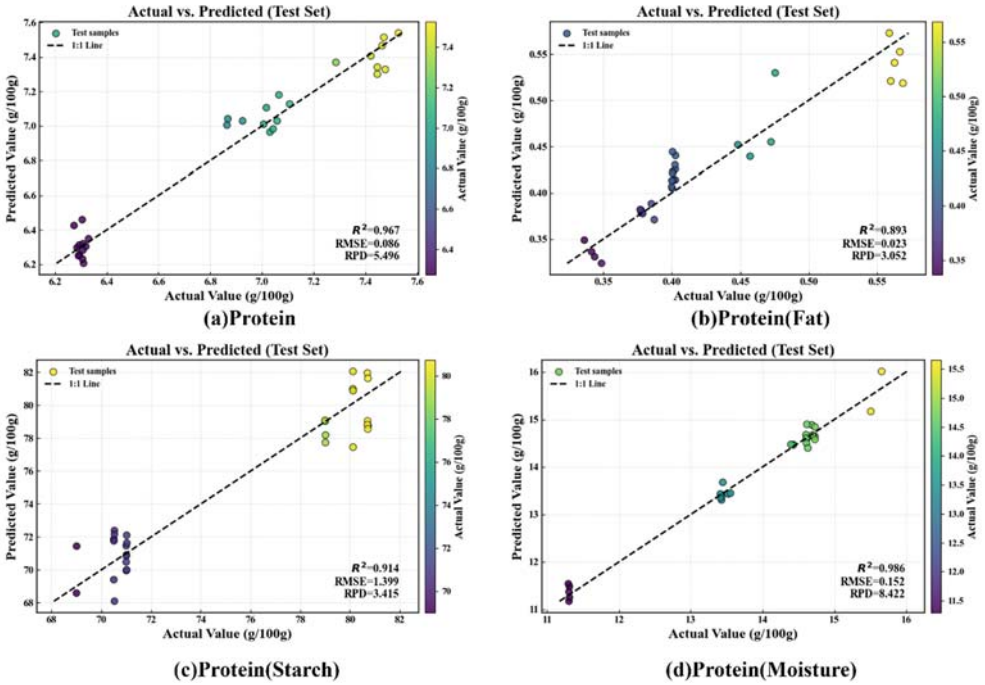


Figure 6. Optimal Results of Physicochemical Fusion Prediction

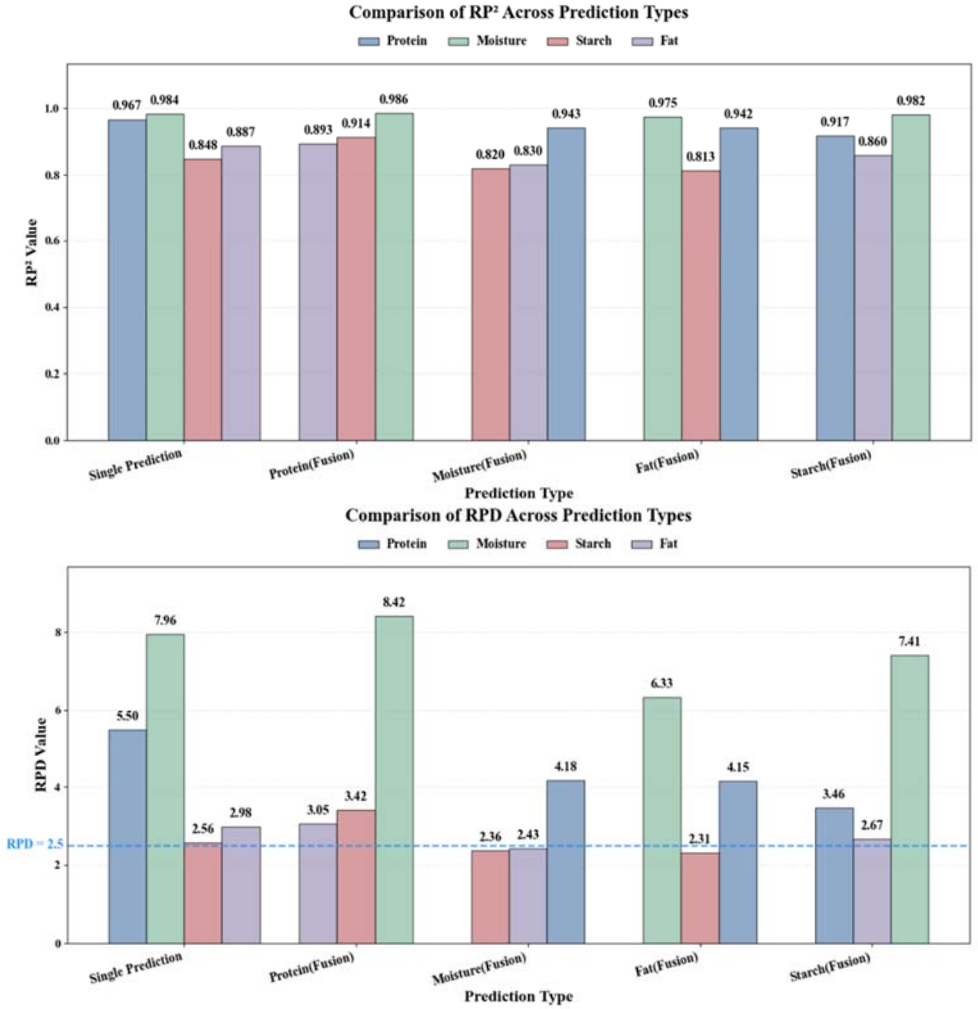


Figure 7. Comparison of Physicochemical Prediction Results (R^2 and RPD)

Figure 8 displays the predicted physicochemical content for the imaged samples. Rows correspond to protein, moisture, fat, and starch, and columns distinguish the samples shown for each component. The color bar for each row defines the value represented by a color; therefore, colors should be compared within a component using its own scale. The maps show variation both between samples and within individual grain images. They provide a spatial view of the model output, complementing the prediction-set statistics in Figure 7, but the apparent patterns remain subject to model error. The maps are useful for identifying samples or regions that merit closer examination. A chemical assay would still be required to confirm the concentration at a particular location. In this sense, visualization is an aid to screening and interpretation rather than independent proof of the distribution of each component.

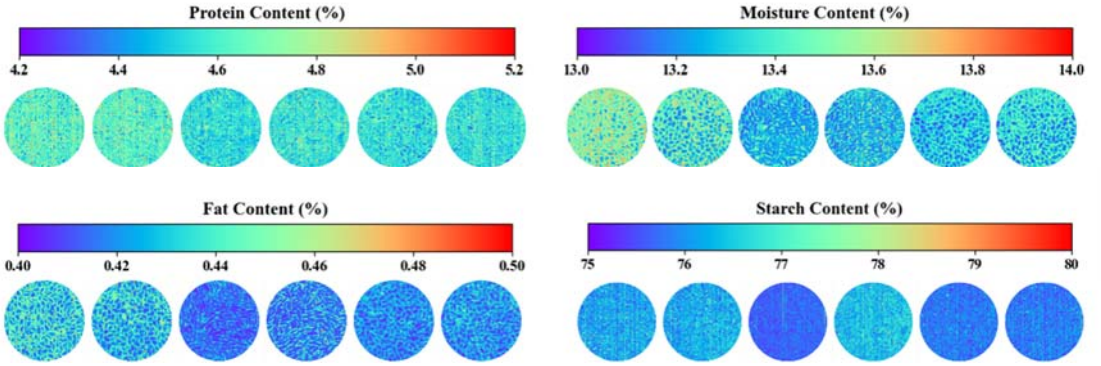


Figure 8. Visualization Results of Physicochemical Contents

4. Conclusions

This study employed HSI technology combined with 1D-CNN and multi-feature fusion to estimate four physicochemical components in glutinous rice. Spectral data were collected from glutinous rice samples across six different regions, and corresponding physicochemical prediction models were developed. The results showed that multi-feature fusion within the 1D-CNN model gave the strongest prediction-set metrics among the configurations tested. The R_P^2 values of all physicochemical indicators exceeded 0.89, and the RPD values were all above 3.0. Among these, moisture achieved the highest prediction performance (R_P^2 = 0.986, RPD = 8.422), the highest reported result among the four components. In comparison, the single-feature 1D-CNN models performed slightly less effectively but still achieved strong predictive ability: the R_P^2 values for protein and moisture both exceeded 0.96, with RPD values above 5.0; fat and starch achieved R_P^2 values above 0.84 and RPD values above 2.5, exhibiting stable overall model performance. In contrast, models based on characteristic wavelengths achieved lower prediction accuracy: the R_P^2 values for protein and moisture were only above 0.84 with RPD values higher than 2.5, whereas fat and starch achieved R_P^2 values above 0.72 and RPD values above 1.9, indicating relatively weaker generalization ability. Therefore, the 1D-CNN model under multi-feature fusion conditions gave higher prediction-set metrics than the spectral-only and selected-wavelength models in this sample set. In summary, combining HSI with a 1D-CNN and using the protein prediction value as the primary fusion feature improved the reported predictions for several components of glutinous rice. The approach may support screening of raw glutinous rice, but independent batches and brewing outcomes must be evaluated before it can be linked to routine process decisions or final liquor quality.

Credit authorship contribution statement

Yuqi Zhou: Writing – original draft, Writing – review & editing. Haili Yang: Supervision. Lei Fei: Resources. Jing Yang: Resources. Hao Xia: Resources. Xinjun Hu, Manjiao Chen: Resources. Dan Huang: Resources. Liangliang Xie: Resources. Haofu Han: Resources.

Conflict of Interest Statement

The authors declare that they do not have any conflict of financial interest.

Funding

This research was supported by the National Engineering Research Center of Solid-State Brewing (grant no. GFGS-2026101996) and the Innovation Fund of Sichuan University of Science & Engineering (grant no. Y2024023).

Data Availability Statement

The data that support the findings of this study are available from the corresponding author upon reasonable request.

Use of Large Language Models, AI and Machine Learning Tools

None declared.

Informed consent

Not applicable.

Research ethics

Not applicable. This study did not involve human participants or animals.

References

[1] Li, H., & Chen, S. (2023). History and advance of flavour research of Baijiu. In Science and Engineering of Chinese Liquor (Baijiu): Microbiology, Chemistry and Process Technology (pp. 163–196). Springer Nature Singapore. https://doi.org/10.1007/978-981-19-2195-7_6.

[2] Wang, Y., Zheng, J., Zhang, D., Pan, S., Xu, X., & Yuan, F. (2025). Flavoromic exploration of regional variations, consumer preferences, and the role of volatile and nonvolatile compounds in strong-aroma Baijiu. Journal of Agricultural and Food Chemistry, 73(28), 17888–17900. https://doi.org/10.1021/acs.jafc.5c05364

[3] Sun, B., Wu, J., & Yu, L. (2021). Chinese National Alcohols: Baijiu and Huangjiu. World Scientific. https://doi.org/10.1142/12190

[4] Xie, P., Shao, M., Deng, X., Ren, Y., Chen, M., Jiang, Y., et al. (2024). Bacterial composition and physicochemical characteristics of sorghum based on environmental factors in different regions of China. Frontiers in Microbiology, 15, 1422471. https://doi.org/10.3389/fmicb.2024.1422471

[5] Zhao, W., Liu, Y., Zhou, K., Li, K., & Shen, J. (2024). How sorghum grain composition affects the quality of Chinese Baijiu - a comprehensive review. Journal of Food Composition and Analysis, 134, 106512. https://doi.org/10.1016/j.jfca.2024.106512

[6] Jie, Z. (2024). Fermentation characteristics and bread baking attributes of bread dough fermented with glutinous rice. Food Science and Applied Microbiology Reports, 2(2), 48–54. https://doi.org/10.61363/fsamr.v1i2.55

[7] Wang, C., Yuan, G., He, Y., Tang, J., Zhou, H., & Qiu, S. (2022). The formation of higher alcohols in rice wine fermentation using different rice cultivars. Frontiers in Microbiology, 13, 978323. https://doi.org/10.3389/fmicb.2022.978323

[8] Li, J., Tang, X., Qian, H., Yang, Y., Zhu, X., Wu, Q., et al. (2021). Analysis of saccharification products of high-concentration glutinous rice fermentation by Rhizopus nigricans Q3 and alcoholic fermentation of Saccharomyces cerevisiae GY-1. ACS Omega, 6(12), 8038–8044. https://doi.org/10.1021/acsomega.0c05452

[9] Huang, T., Ouyang, D., Sang, S., Li, C., Wang, X., Wang, X., et al. (2024). Effect of water content in semidry grinding on the quality of glutinous rice flour. Foods, 13(20), 3216. https://doi.org/10.3390/foods13203216

[10] Jiang, Y., Sun, J., Yin, Z., Li, H., Sun, X., & Zheng, F. (2020). Evaluation of antioxidant peptides generated from Jiuzao (residue after Baijiu distillation) protein hydrolysates and their effect of enhancing healthy value of Chinese Baijiu. Journal of the Science of Food and Agriculture, 100(1), 59–73. https://doi.org/10.1002/jsfa.9994

[11] Wang, Y., Yu, K., Xiao, X., Tan, J., Liao, R., Li, C., et al. (2025). Influence of glutinous rice raw material characteristics on the aroma profile of rice wine. Molecules, 30(16), 3315. https://doi.org/10.3390/molecules30163315

[12] He, B., Zhang, C., Cao, X., Li, G., & Xiong, X. (2023). An approach to recognizing the working cycle stage with small sample data for energy conservation. Journal of Cleaner Production, 414, 137771. https://doi.org/10.1016/j.jclepro.2023.137771

[13] Song, D., Zhong, X., Wu, Y., Guo, J., Song, L., & Yang, L. (2025). From artisan experience to scientific elucidation: preparation processes, microbial diversity, and food applications of Chinese traditional fermentation starters (Qu). Foods, 14(22), 3814. https://doi.org/10.3390/foods14223814

[14] Yang, J., Shen, G., & Qin, J. (2025). Non-destructive sensing of nitrogen and phosphorus contents in plants via hyperspectral imaging of Hydrangea macrophylla at the seeding stage. Scientia Horticulturae, 347, 114144. https://doi.org/10.1016/j.scienta.2025.114144

[15] He, K., Tian, J., Xia, Y., Zhou, Y., Hu, X., Xie, L., et al. (2025). Detection of the amylose and amylopectin contents of rice by hyperspectral imaging combined with a CNN-AdaBoost model. Journal of Food Composition and Analysis, 142, 107468. https://doi.org/10.1016/j.jfca.2025.107468

[16] Zhong, H., Chai, J., Yu, C., Wang, K., Wang, K., & Lin, P. (2025). Rapid detection of oil content in Camellia oleifera kernels based on hyperspectral imaging and machine learning. Journal of Food Composition and Analysis, 137, 106899. https://doi.org/10.1016/j.jfca.2024.106899

[17] Li, X., Wang, D., Gong, J., Yu, L., Ma, F., Wang, X., et al. (2025). Rapid and nondestructive detection of oil content and fatty acids of soybean using hyperspectral imaging. Journal of Food Composition and Analysis, 139, 107033. https://doi.org/10.1016/j.jfca.2024.107033

[18] Manea, D., & Calin, M. A. (2015). Hyperspectral imaging in different light conditions. The Imaging Science Journal, 63(4), 214–219. https://doi.org/10.1179/1743131X15Y.0000000001

[19] Davies, M., Stuart, M. B., Hobbs, M. J., McGonigle, A. J. S., & Willmott, J. R. (2022). Image correction and in situ spectral calibration for low-cost, smartphone hyperspectral imaging. Remote Sensing, 14(5), 1152. https://doi.org/10.3390/rs14051152

[20] Xue, X., Tian, H., Zhao, K., Yu, Y., Xiao, Z., Zhuo, C., et al. (2024). Rapid lactic acid content detection in secondary fermentation of maize silage using colorimetric sensor array combined with hyperspectral imaging. Agriculture, 14(9), 1653. https://doi.org/10.3390/agriculture14091653

[21] Liu, X., Wu, Z., Zhao, Q., Yu, Y., & Li, Z. (2025). Using near-infrared hyperspectral imaging combined with machine learning to predict the components and the origin of Radix Paeoniae Rubra. Analytical Methods, 17(6), 1334–1344. https://doi.org/10.1039/D4AY01977F

[22] Sun, X., Zhou, X., Liu, C., Li, C., Zhang, S., & Zheng, D. (2025). Rapid and nondestructive identification of rice storage year using hyperspectral technology. Food Control, 168, 110850. https://doi.org/10.1016/j.foodcont.2024.110850

[23] Awad, M., & Khanna, R. (2015). Support vector regression. In Efficient Learning Machines: Theories, Concepts, and Applications for Engineers and System Designers (pp. 67–80). Apress. https://doi.org/10.1007/978-1-4302-5990-9_4

[24] Chen, T., & Guestrin, C. (2016). XGBoost: a scalable tree boosting system. In Proceedings of the 22nd ACM SIGKDD International Conference on Knowledge Discovery and Data Mining (pp. 785–794). Association for Computing Machinery. https://doi.org/10.1145/2939672.2939785

[25] Hu, H., Mei, Y., Wei, Y., Xu, Z., Zhao, Y., Xu, H., et al. (2024). Chemical composition prediction in goji (Lycium barbarum) using hyperspectral imaging and multi-task 1DCNN with attention mechanism. LWT, 204, 116436. https://doi.org/10.1016/j.lwt.2024.116436

[26] Analla, M. (1998). Model validation through the linear regression fit to actual versus predicted values. Agricultural Systems, 57(1), 115–119. https://doi.org/10.1016/S0308-521X(97)00073-5

[27] Meng, Q., Tan, T., Feng, S., Wen, Q., & Shang, J. (2024). Prediction and visualization map for physicochemical indices of kiwifruits by hyperspectral imaging. Frontiers in Nutrition, 11, 1364274. https://doi.org/10.3389/fnut.2024.1364274

[28] Ekramirad, N., Khaled, A. Y., Doyle, L. E., Loeb, J. R., Donohue, K. D., Villanueva, R. T., et al. (2021). Nondestructive detection of codling moth infestation in apples using pixel-based NIR hyperspectral imaging with machine learning and feature selection. Foods, 11(1), 8. https://doi.org/10.3390/foods11010008

[29] Li, J., Luo, W., Wang, Z., & Fan, S. (2019). Early detection of decay on apples using hyperspectral reflectance imaging combining both principal component analysis and improved watershed segmentation method. Postharvest Biology and Technology, 149, 235–246. https://doi.org/10.1016/j.postharvbio.2018.12.007

[30] Wang, Z., Fan, S., Wu, J., Zhang, C., Xu, F., Yang, X., et al. (2021). Application of long-wave near infrared hyperspectral imaging for determination of moisture content of single maize seed. Spectrochimica Acta Part A: Molecular and Biomolecular Spectroscopy, 254, 119666. https://doi.org/10.1016/j.saa.2021.119666

[31] Dufera, A. G., Liu, T., & Xu, J. (2023). Regression models of Pearson correlation coefficient. Statistical Theory and Related Fields, 7(2), 97–106. https://doi.org/10.1080/24754269.2023.2164970.